scientific reports

Check for updates

OPEN

Identification of $G\alpha_{12}$-vs-$G\alpha_{13}$-coupling determinants and development of a $G\alpha_{12/13}$-coupled designer GPCR

Manae Tatsumi[1], Christian Cruz[2], Nozomi Kamakura[1], Riku Kuwabara[1], Gaku Nakamura[1], Tatsuya Ikuta[1], Ravinder Abrol[2] & Asuka Inoue[1,3]✉

G-protein-coupled receptors (GPCRs) transduce diverse signals into the cell by coupling to one or several Gα subtypes. Of the 16 Gα subtypes in human cells, $G\alpha_{12}$ and $G\alpha_{13}$ belong to the G_{12} subfamily and are reported to be functionally different. Notably, certain GPCRs display selective coupling to either $G\alpha_{12}$ or $G\alpha_{13}$, highlighting their significance in various cellular contexts. However, the structural basis underlying this selectivity remains unclear. Here, using a $G\alpha_{12}$-coupled designer receptor exclusively activated by designer drugs (DREADD; $G_{12}D$) as a model system, we identified residues in the α5 helix and the receptor that collaboratively determine $G\alpha_{12}$-vs-$G\alpha_{13}$ selectivity. Residue-swapping experiments showed that $G_{12}D$ distinguishes differences between $G\alpha_{12}$ and $G\alpha_{13}$ in the positions G.H5.09 and G.H5.23 in the α5 helix. Molecular dynamics simulations observed that $I378^{G.H5.23}$ in $G\alpha_{12}$ interacts with $N103^{2.39}$, $S169^{3.53}$ and $Y176^{34.53}$ in $G_{12}D$, while $H364^{G.H5.09}$ in $G\alpha_{12}$ interact with $Q264^{5.71}$ in $G_{12}D$. Screening of mutations at these positions in $G_{12}D$ identified $G_{12}D$ mutants that enhanced coupling with $G\alpha_{12}$ and to an even greater extent with $G\alpha_{13}$. Combined mutations, most notably the dual $Y176^{34.53}H$ and $Q264^{5.71}R$ mutant, further enhanced $G\alpha_{12/13}$ coupling, thereby serving as a potential $G\alpha_{12/13}$-DREADD. Such novel $G\alpha_{12/13}$-DREADD may be useful in future efforts to develop drugs that target $G\alpha_{12/13}$ signaling as well as to identify their therapeutic indications.

G-protein-coupled receptors (GPCRs) are the largest superfamily of membrane proteins and are involved in virtually all physiological phenomena[1,2]. GPCRs regulate intracellular pathways by binding extracellular ligands and transmitting signals across the plasma membrane to intracellular effector molecules via heterotrimeric G proteins composed of Gα, Gβ, and Gγ subunits[3]. The 16 Gα subtypes in human cells are classified into four Gα subfamilies ($G\alpha_s$, $G\alpha_i$, $G\alpha_q$, and $G\alpha_{12}$) that transmit unique signals (e.g., cAMP, Ca^{2+}, inositol phosphate, and Rho activation) and Gα subtypes belonging to each of these subfamilies have been thought to exert similar functions[1]. However, recent studies have revealed that subtypes belonging to the same subfamily have different patterns of coupling to GPCRs and exert distinct functions, requiring further analysis focusing on each subtype[4–6].

$G\alpha_{12}$ and $G\alpha_{13}$, which belong to the G_{12} subfamily, activate the small GTPase Rho through Rho-specific guanine nucleotide exchange factors[7]. Some reports indicate that $G\alpha_{12}$ and $G\alpha_{13}$ are functionally different, interacting with different effector target proteins leading to different outcomes. For example, $G\alpha_{13}$-knockout mice are embryonic lethal due to defective angiogenesis, whereas $G\alpha_{12}$ knockout mice develop normally despite the expression of both subtypes in the vascular endothelial cells[8–10]. This phenotypic difference has been attributed to myocyte-specific enhancer factor-2 (MEF2), which is specifically activated downstream of $G\alpha_{13}$[11]. Several other effector proteins, such as Hsp90 and PYK2, have been identified to bind specifically to $G\alpha_{12}$ or $G\alpha_{13}$, respectively[12,13].

Some GPCRs selectively couple to either $G\alpha_{12}$ or $G\alpha_{13}$, indicating that they are used effectively in various physiological conditions. In our previous study, we generated a dataset quantifying the coupling of 11 chimeric Gα proteins including $G\alpha_{12}$ and $G\alpha_{13}$ to 148 GPCRs by using TGFα shedding assay[5]. A meta-analysis integrating this dataset with the Guide to Pharmacology and the Bouvier datasets showed that 25 GPCRs were found to be coupled to both $G\alpha_{12}$ and $G\alpha_{13}$, 5 GPCRs specifically to $G\alpha_{12}$, and 8 GPCRs specifically to $G\alpha_{13}$[5,14–16]. However, it remains uncertain how GPCRs interact with $G\alpha_{12}$ or $G\alpha_{13}$ and what determines their coupling selectivity.

[1]Graduate School of Pharmaceutical Sciences, Tohoku University, 6-3, Aoba, Aramaki, Aoba-ku, Sendai, Miyagi 980-8578, Japan. [2]Department of Chemistry and Biochemistry, California State University, Northridge, CA 91330, USA. [3]Present address: Graduate School of Pharmaceutical Sciences, Kyoto University, 46-29 Yoshida-Shimo-Adachi-cho, Sakyo-ku, Kyoto 606-8501, Japan. ✉email: iaska@tohoku.ac.jp

The C-terminal helix (α5 helix) of the Gα subunits is an important determinant for coupling selectivity. The α5 helix consists of 26 amino acids and interacts with the transmembrane core of GPCRs, occupying > 70% of the GPCR–G protein interface. Structural studies of the GPCR–Gα protein complex and cell-based assays confirmed the role of the α5 helix in determining Gα coupling selectivity[17–19]. In GPR35, out of the eight amino acids of the α5 helix that differ between $Gα_{12}$ and $Gα_{13}$, G.H5.23, the fourth residue from the C-terminus of the Gα subunit, contributes to its $Gα_{13}$ preference over $Gα_{12}$[20]. Thus, focusing on the interaction between a receptor and the α5 helix would help determine the key elements regulating the coupling selectivity between $Gα_{12}$ and $Gα_{13}$.

We have previously generated a $Gα_{12}$-coupled Designer Receptor Exclusively Activated by Designer Drugs (DREADD) through a series of modifications. The first generation of $Gα_{12}$-coupled DREADD was designed by modifying $Gα_q$-coupled DREADD (M3D) based on the TGFα shedding assay database[5,21]. Subsequently, an $F93^{1.57}V$ mutation was introduced into the first-generation DREADD to create a second-generation $Gα_{12}$-DREADD ($G_{12}D$), which couples strongly to $Gα_{12}$ but weakly to $Gα_{13}$[22]. In the present study, we used the second generation $G_{12}D$ as an experimental model for analyzing the mechanism and determinants of $Gα_{12}$-vs-$Gα_{13}$-coupling selectivity.

In this study, by utilizing chimeric Gα proteins, we identified the specific residues in the α5 helix of $Gα_{12}$ responsible for $Gα_{12}$ selectivity. Through molecular dynamics analysis, we pinpointed residues in $G_{12}D$ that involve interactions with the selectivity determinants in the α5 helix. Finally, by mutating $G_{12}D$, we successfully developed a $Gα_{12/13}$-DREADD that increased both $Gα_{12/13}$ coupling to similar extents.

Results

The $Gα_{12}$ selectivity of $G_{12}D$ requires specific amino acid residues in the α5 helix including isoleucine G.H5.23

To determine which amino acid residues in the α5 helix are critical for preferential coupling for $Gα_{12}$ over $Gα_{13}$ by $G_{12}D$, we constructed chimeric Gα proteins, in which the α5 helix (G.H5.01–G.H5.26) of $Gα_q$ was replaced by the α5 helix of $Gα_{12}$ or $Gα_{13}$ ($Gα_{q\text{-}12C}$ or $Gα_{q\text{-}13C}$, respectively). By following a previous strategy[5] where we introduced a chimeric Gα subunit in the $Gα_q/Gα_{11}/Gα_{12}/Gα_{13}$ quadruple-deficient HEK293 cells ($ΔG_q/ΔG_{12}$ cells), we herein co-expressed $Gα_{q\text{-}12C}$ or $Gα_{q\text{-}13C}$ along with $G_{12}D$ and a reporter gene encoding alkaline phosphatase-tagged TGFα (AP-TGFα) in $ΔGq/ΔG_{12}$ cells. Cells were stimulated with increasing concentrations of clozapine-N-oxide (CNO) and the relative coupling of $Gα_{q\text{-}12C}$ and $Gα_{q\text{-}13C}$ to $G_{12}D$ was evaluated by measuring the activity of cleaved AP-TGFα (Fig. 1A,B). The relative intrinsic activities (RAi) of $Gα_{q\text{-}13C}$ to $Gα_{q\text{-}12C}$ was calculated from the concentration–response curves in the TGFα shedding assay[5,23]. This parameter analysis showed that the RAi was 4.6-fold higher in cells expressing $Gα_{q\text{-}12C}$ than in cells expressing $Gα_{q\text{-}13C}$, confirming a previous report that $G_{12}D$ preferentially couples with $Gα_{q\text{-}12C}$[5] (Fig. 1C). The amino acid sequences of the α5 helices of $Gα_{12}$ and $Gα_{13}$ differ at the following positions: G.H5.04, G.H5.06, G.H5.09, G.H5.10, G.H5.17, G.H5.18, G.H5.22, and G.H5.23 (Fig. 1D). To determine which of these amino acid differences confer coupling selectivity, we constructed eight pairs of chimeric Gα protein mutants. Specifically, the amino acid at one of the eight variable positions in the α5 helix was switched from its $Gα_{12}$ residue to its $Gα_{13}$ residue or vice versa, while the rest of the $Gα_{q\text{-}12C}$ and $Gα_{q\text{-}13C}$ protein sequences remained unchanged (Fig. 1E, Supplementary Fig. 1). We found that coupling selectivity was reversed when the amino acid at the position G.H5.23 was reversed; thus, $Gα_{q\text{-}13C}$ carrying a leucine to isoleucine mutation (*i.e.*, $Gα_{q\text{-}13C}$ [$L^{G.H5.23}I$]) coupled preferentially to $G_{12}D$, while the reverse mutants, $Gα_{q\text{-}12C}$ ($I^{G.H5.23}L$), did not (Fig. 1F,G, Supplementary Fig. 2). In addition, $Gα_{q\text{-}13C}$ ($R^{G.H5.09}H$) enhanced coupling with $G_{12}D$, while $Gα_{q\text{-}12C}$ ($H^{G.H5.09}R$) tended to decrease it (Fig. 1F,G, Supplementary Fig. 2). These results indicate that $Gα_{12}$ and $Gα_{13}$ coupling specificity is attributable to the specific residues in the α5 helix, most notably at the position G.H5.23 (isoleucine and leucine, respectively).

MD simulations reveal interactions involving $Gα_{12}$ selectivity of $G_{12}D$

To gain insight into the $Gα_{12}$ selectivity of $G_{12}D$, we performed molecular dynamics (MD) simulations of the $G_{12}D$–$Gα_{12}$ and the $G_{12}D$–$Gα_{13}$ complexes. The two complexes were modeled with SWISS-MODEL and I-TASSER structure prediction software using M1R–$Gα_{11}$ complex structure (PDB: 6OIJ) as a template and embedded into lipid bilayers using CHARMM-GUI[24–27] (Fig. 2A). Both models were simulated for 500 ns using a conventional MD protocol to estimate the Poisson-Boltzmann-based energy of the Gα protein to the receptor as described previously[28]. Because calculations of the $G_{12}D$–$Gα_{12}$ total energy indicated that low energy states were not conformationally sampled, 500-ns Gaussian Accelerated Molecular Dynamics (GaMD) simulations were performed[29]. The GaMD snapshots of the $G_{12}D$–$Gα_{12}$ complex clustered into two distinct conformations and the snapshots of the $G_{12}D$–$Gα_{13}$ complex clustered into five distinct conformations, indicating that the latter complex was more dynamic. The average structure that best represented each cluster was then chosen as the starting point for a final 500-ns conventional MD allowing for unbiased free energy calculations and receptor–G protein interaction analyses. For the $G_{12}D$–$Gα_{12}$ complex, most structural variation between the two clusters was in the internal dynamics of the $Gα_{12}$ protein and TM6 of the receptor. For the $G_{12}D$–$Gα_{13}$ complex, most structural variation among the five clusters was in the internal dynamics of the $Gα_{13}$ protein, the positioning of its α5 helix, and the intracellular facing regions of TM5/TM6 domains of the receptor.

The results of the MD simulations revealed significant differences in the stability of $Gα_{12}$ and $Gα_{13}$ interaction with $G_{12}D$. From the MD trajectories, we calculated the total energy (ΔG) of $Gα_{12}$ and $Gα_{13}$ through MMPBSA analysis[30]. We found that ΔG was weaker (less negative) in the $Gα_{13}$ simulation than in the $Gα_{12}$ simulation, indicating that the interaction between $G_{12}D$ and $Gα_{13}$ is less stable than that between $G_{12}D$ and $Gα_{12}$ (Fig. 2A). We also observed that the position in the α5 helix of $Gα_{13}$ in the transmembrane core of $G_{12}D$ was variable, while its position in $Gα_{12}$ was more stable and essentially stayed in the transmembrane core of $G_{12}D$ (Fig. 2B). Indeed, the root-mean-square deviation (RMSD) for the α5 helix was higher in the $Gα_{13}$ simulation than in the $Gα_{12}$

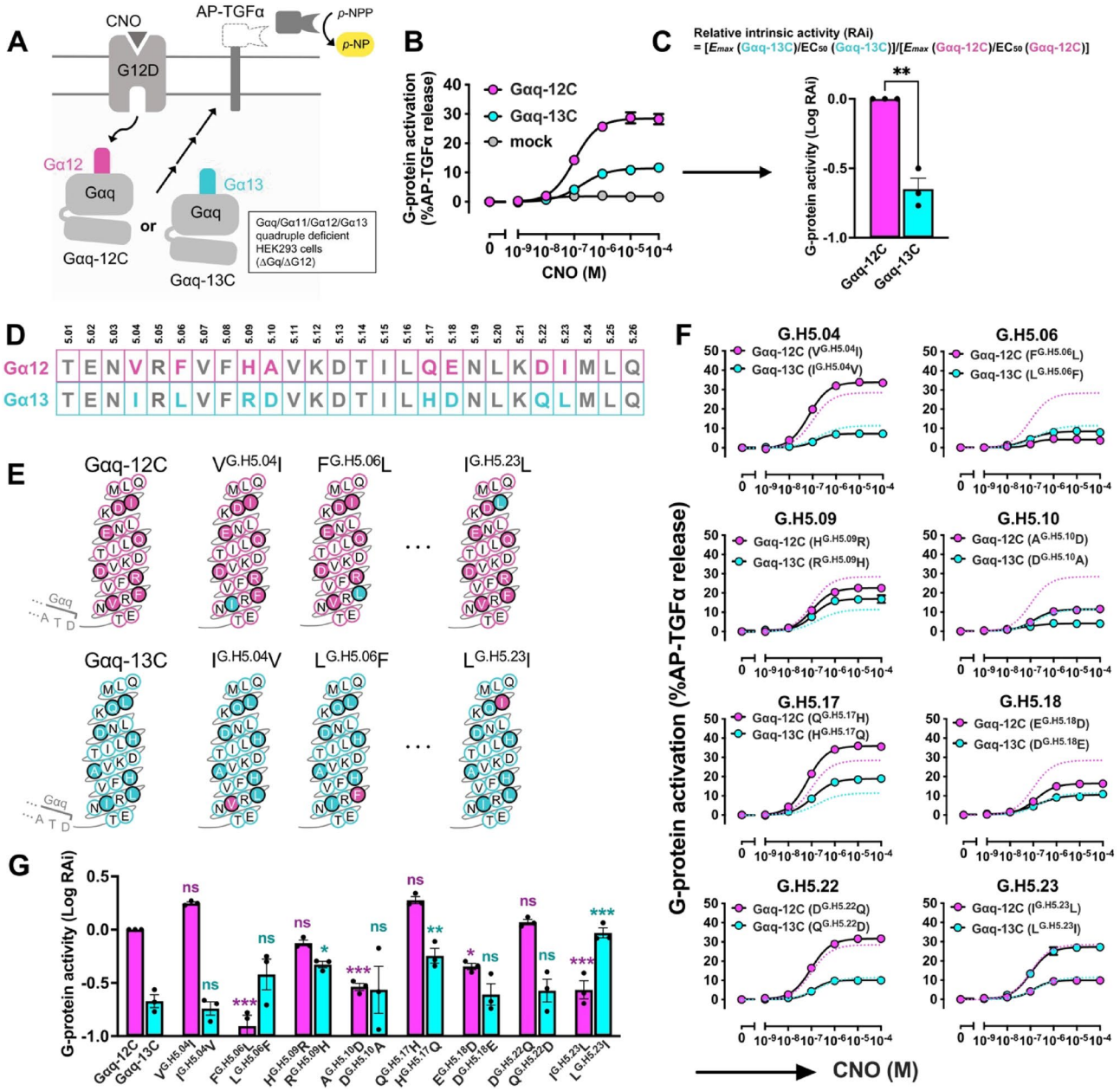

Figure 1. Identification of residues in the α5 helix involved in the $G\alpha_{12}$-vs-$G\alpha_{13}$-coupling selectivity by the TGFα shedding assay. (**A**) Schematic representation of the TGFα shedding assay for evaluating coupling between $G_{12}D$ and $G\alpha_{q\text{-}12C}$ or $G\alpha_{q\text{-}13C}$. $G_{12}D$, chimeric Gα ($G\alpha_{q\text{-}12C}$ or $G\alpha_{q\text{-}13C}$), and AP-TGFα are transiently expressed in $\Delta G_q/\Delta G_{12}$ cells. Upon stimulation with CNO, $G_{12}D$ is coupled with the chimeric Gα, of which activation leads to ectodomain shedding of the AP-TGFα reporter. Cleaved AP-TGFα is quantified by measuring AP activity in the conditioned media based on the production of para-nitrophenol (*p*-NP) from para-nitrophenyl phosphate (*p*-NPP). See the method section for detail. (**B**) Concentration–response curve for the TGFα shedding responses induced by $G_{12}D$ activation upon CNO stimulation. The vehicle-treated condition is set as the baseline. The magenta and cyan circles represent the response under conditions expressing $G\alpha_{q\text{-}12C}$ and $G\alpha_{q\text{-}13C}$, respectively. (**C**) Logarithmic values of relative intrinsic activity (RAi) calculated from (B) using the formula shown in the figure. The values were normalized by the $G\alpha_{q\text{-}12C}$ expressing condition. Bars and error bars represent the mean and SEM, respectively, for three independent experiments with each dot representing an individual experiment. ** represents $P < 0.01$ with the two-tailed *t*-test. (**D**) Amino acid sequence of the α5 helices of $G\alpha_{12}$ and $G\alpha_{13}$. Positions where amino acids differ between $G\alpha_{12}$ and $G\alpha_{13}$ are highlighted in magenta and cyan, respectively. (**E**) Design of swapped mutants in the $G\alpha_{q\text{-}12C}$ and the $G\alpha_{q\text{-}13C}$ backbones. Mutants in positions G.H5.09, G.H5.10, G.H5.17, G.H5.18, and G.H5.22 are omitted. (**F**) Concentration–response curve for the TGFα shedding responses of the swapped mutants. The dashed lines represent the responses of $G\alpha_{q\text{-}12C}$ (magenta) and $G\alpha_{q\text{-}13C}$ (cyan) shown in (B). In all panels, the symbols and error bars represent the mean and SEM, respectively, for three independent experiments performed in triplicate. For many data points, the error bars are smaller than the symbols and, thus, are not visible. (**G**) Logarithmic values of RAi of the swapped mutants calculated from (F). Bars and error bars represent the mean and SEM, respectively, for three independent experiments with each dot representing an individual experiment. ns, *, ** and *** represent $P > 0.05$, < 0.05, < 0.01 and < 0.001, respectively, with two-way ANOVA, followed by the Dunnett's multiple comparisons test ($G\alpha_{q\text{-}12}$ mutants with wild-type $G\alpha_{q\text{-}12C}$; $G\alpha_{q\text{-}13}$ mutants with wild-type $G\alpha_{q\text{-}13C}$).

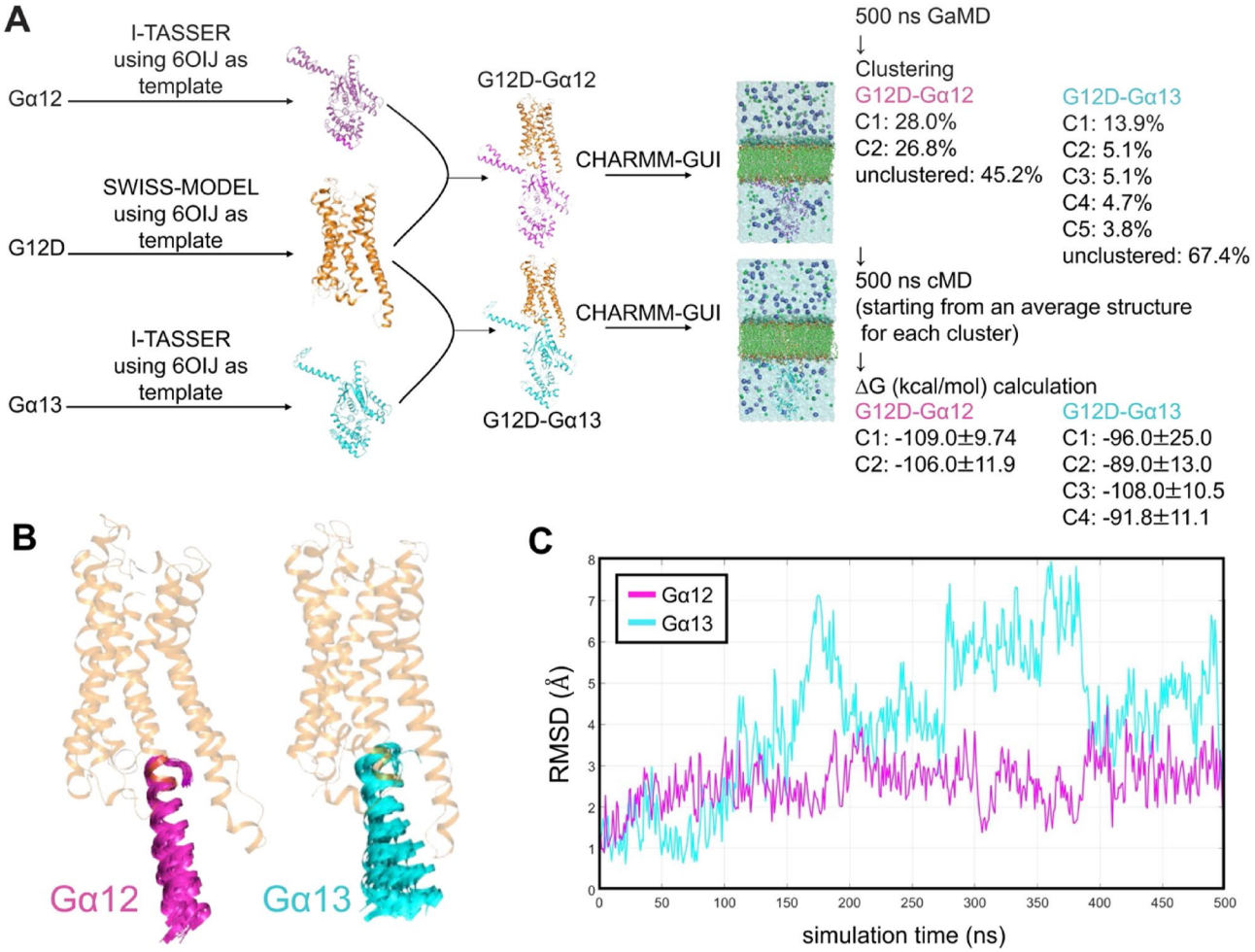

Figure 2. Comparison of the stability between the $G_{12}D$–$G\alpha_{12}$ and the $G_{12}D$–$G\alpha_{13}$ complexes through MD simulations. (**A**) Schematic representation of the molecular dynamics simulations. On the right side, the occupancy (%) of each cluster and the ΔG (kcal/mol) calculated from the cMD results are displayed. (**B**) Overlap of snapshots every 20 ns from 500-ns cMD simulations starting from each cluster 1 (C1). For clarity, $G_{12}D$ is shown with the average structure of each simulation and residues other than the α5 helix are hidden. (**C**) RMSD for the α5 helix calculated from 500-ns cMD simulations starting from C1.

simulation for the most populated cluster (C1; Fig. 2C). RMSD analysis for the α5 helix for all clusters showed that, compared with the C1 cluster of the $G_{12}D$–$G\alpha_{12}$ complex, all of the other clusters including those of the $G_{12}D$–$G\alpha_{13}$ complex were sampled more frequently in positions with RMSD scores beyond 4 Å (Supplementary Fig. 3A). These observations are consistent with the results of cell-based assays (Fig. 1F,G).

The most notable differences in the simulations of the $G_{12}D$–$G\alpha_{12}$ and the $G_{12}D$–$G\alpha_{13}$ complexes were in ICL2. More specifically, when comparing the average structures of the two complexes, the position of ICL2 was tilted 3.5 Å more toward the α5 helix in the $G_{12}D$–$G\alpha_{12}$ complex than in the $G_{12}D$–$G\alpha_{13}$ complex (Fig. 3A). Among residues in the ICL2, $Y176^{34.53}$ showed the most noticeable difference between the simulations (Fig. 3B). In the simulation of the $G_{12}D$–$G\alpha_{12}$ complex, $Y176^{34.53}$ was positioned between $N103^{2.39}$ and $S169^{3.53}$ and oriented toward $G\alpha_{12}$ residue $I^{G.H5.23}$, such that $Y176^{34.53}$, $N103^{2.39}$, and $S169^{3.53}$ form a pocket for the methyl group of $I^{G.H5.23}$ (Fig. 3B,C, Supplementary Fig. 3B). These observations show that the transmembrane core of $G_{12}D$ contains a pocket that accommodates $I^{G.H5.23}$, and this likely stabilizes the $G_{12}D$–$G\alpha_{12}$ complex in a low energy state. On the other hand, in the α5 helix of $G\alpha_{13}$, $L^{G.H5.23}$ appeared disoriented and tilted toward TM5 and TM6 (Fig. 3D), while $G_{12}D$ $Y176^{34.53}$ was oriented upward and failed to form a pocket with $N103^{2.39}$ and $S169^{3.53}$, likely disfavoring an interaction between these residues and $G\alpha_{13}$ $L^{G.H5.23}$ (Fig. 3D, Supplementary Fig. 3B). Together, these observations suggest that the pocket formed by $G_{12}D$ residues $N103^{2.39}$, $S169^{3.53}$ and $Y176^{34.53}$ plays a significant role in the preferential coupling between $G_{12}D$ and $G\alpha_{12}$.

In the $G_{12}D$ structures, we found another difference in the region composed of the C-terminal portion of the TM5, ICL3 and the N-terminal portion of TM6 (TM5–ICL3–TM6). In the simulation of the $G_{12}D$–$G\alpha_{12}$ complex, the TM5–ICL3–TM6 region was located farther from the transmembrane core side than in the $G\alpha_{13}$ simulation (Fig. 3E). In general, the active form of GPCR displays an outward shift of TM5–ICL3–TM6, which facilitates the accommodation of α5 helix[17]. Therefore, the TM5–ICL3–TM6 opening observed in the $G_{12}D$–$G\alpha_{12}$ complex

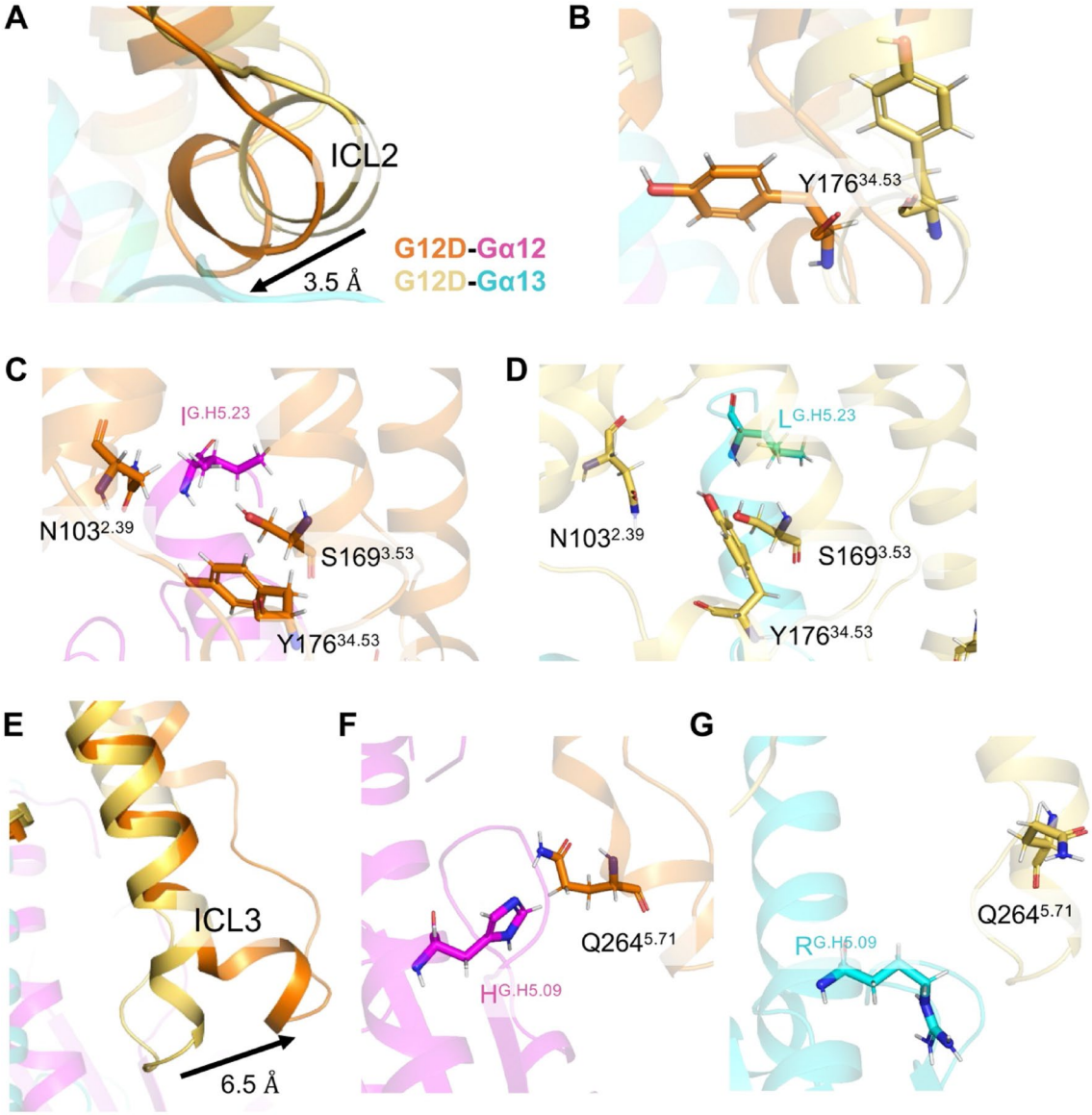

Figure 3. Structural comparison of the $G_{12}D$–$G\alpha_{12}$ and the $G_{12}D$–$G\alpha_{13}$ complexes through MD simulations. (**A**) A comparison of ICL2 structures between the $G_{12}D$–$G\alpha_{12}$ and the $G_{12}D$–$G\alpha_{13}$ complexes. Shown are representative structures during the 500-ns cMD simulations of the $G_{12}D$ complexes, each started from the most populated clusters (C1) observed in the GaMD simulations. These structures were aligned with $G_{12}D$ transmembrane bundles. In the $G_{12}D$–$G\alpha_{12}$ complex, $G_{12}D$ and $G\alpha_{12}$ are shown in orange and magenta, respectively. In the $G_{12}D$–$G\alpha_{13}$ complex, $G_{12}D$ and $G\alpha_{12}$ are shown in yellow and cyan, respectively. (**B**) A comparison of the positions of $Y176^{34.53}$ between the $G_{12}D$–$G\alpha_{12}$ and the $G_{12}D$–$G\alpha_{13}$ complexes. (**C**,**D**) Detailed positions of $G\alpha_{12}$ $Ile^{G.H5.23}$ (C) and $G\alpha_{13}$ $Leu^{G.H5.23}$ (D) in the transmembrane core of $G_{12}D$. (**E**) A comparison of ICL3 structures between the $G_{12}D$–$G\alpha_{12}$ and the $G_{12}D$–$G\alpha_{13}$ complexes. (**F**,**G**) Detailed orientations of G.H5.09 residue.

likely reflects a favorable form for coupling. In the simulations, TM5–ICL3–TM6 was in the proximity of the G.H5.09 residue position out of the eight different residues in the α5 helices of $G\alpha_{12}$ and $G\alpha_{13}$. Consistent with the observations, in the mutant experiment in Fig. 1E,F, the mutants in which these positions of $G\alpha_{13}$ were swapped for $G\alpha_{12}$ residues showed enhanced coupling to $G_{12}D$, indicating their involvement in the selectivity. In the simulations, the G.H5.09 residue appeared to be closest to $Q264^{5.71}$ in $G_{12}D$ (Fig. 3F,G). Therefore, $Q264^{5.71}$, in addition to the previously mentioned $N103^{2.39}$, $S169^{3.53}$ and $Y176^{34.53}$, are potential residues involved in the selectivity.

$N103^{2.39}$, $S169^{3.53}$, $Y176^{34.53}$ and $Q264^{5.71}$ in $G_{12}D$ collectively contribute to the $G\alpha_{12}$-vs-$G\alpha_{13}$ selectivity

To examine the importance $N103^{2.39}$, $S169^{3.53}$, $Y176^{34.53}$ and $Q264^{5.71}$ in the $G\alpha_{12}$-vs-$G\alpha_{13}$-coupling selectivity as well as to generate a $G_{12}D$ mutant with enhanced $G\alpha_{13}$ coupling, we next performed mutation studies in $G_{12}D$. We engineered 19 amino acid substitution mutations at these positions and examined the coupling of $G\alpha_{12}$ and

$G\alpha_{13}$ for a total of 76 mutants. Each $G_{12}D$ mutant carried an N-terminal FLAG-epitope tag to allow cell surface expression to be quantified by flow cytometry. Most mutants carrying substitutions of $N103^{2.39}$ and $Y176^{34.53}$ were expressed at a lower level than the wild-type (WT) control, while expression of mutants carrying substitutions of $S169^{3.53}$ and $Q264^{5.71}$ showed relatively smaller changes in expression level (Supplementary Fig. 4). Next, the $G\alpha_{12}$-vs-$G\alpha_{13}$ selectivity of these mutants was assessed using the TGFα shedding assay. The RAi values were calculated using the equation shown in Fig. 4A, offering indexes into the extent to which the mutants enhanced (or reduced) coupling to $G\alpha_{q\text{-}12C}$ and $G\alpha_{q\text{-}13C}$ relative to the wild-type $G_{12}D$ (Fig. 4B,C, Supplementary Fig. 5–9). $G_{12}D$ mutants — with substitutions at $N103^{2.39}$ with R, K or P; $Y176^{34.53}$ with H, S, A or W; or $Q264^{5.71}$ with R or P — showed higher RAi and stronger coupling to $G\alpha_{q\text{-}12C}$ and $G\alpha_{q\text{-}13C}$ than WT. In particular, $Y176^{34.53}$H

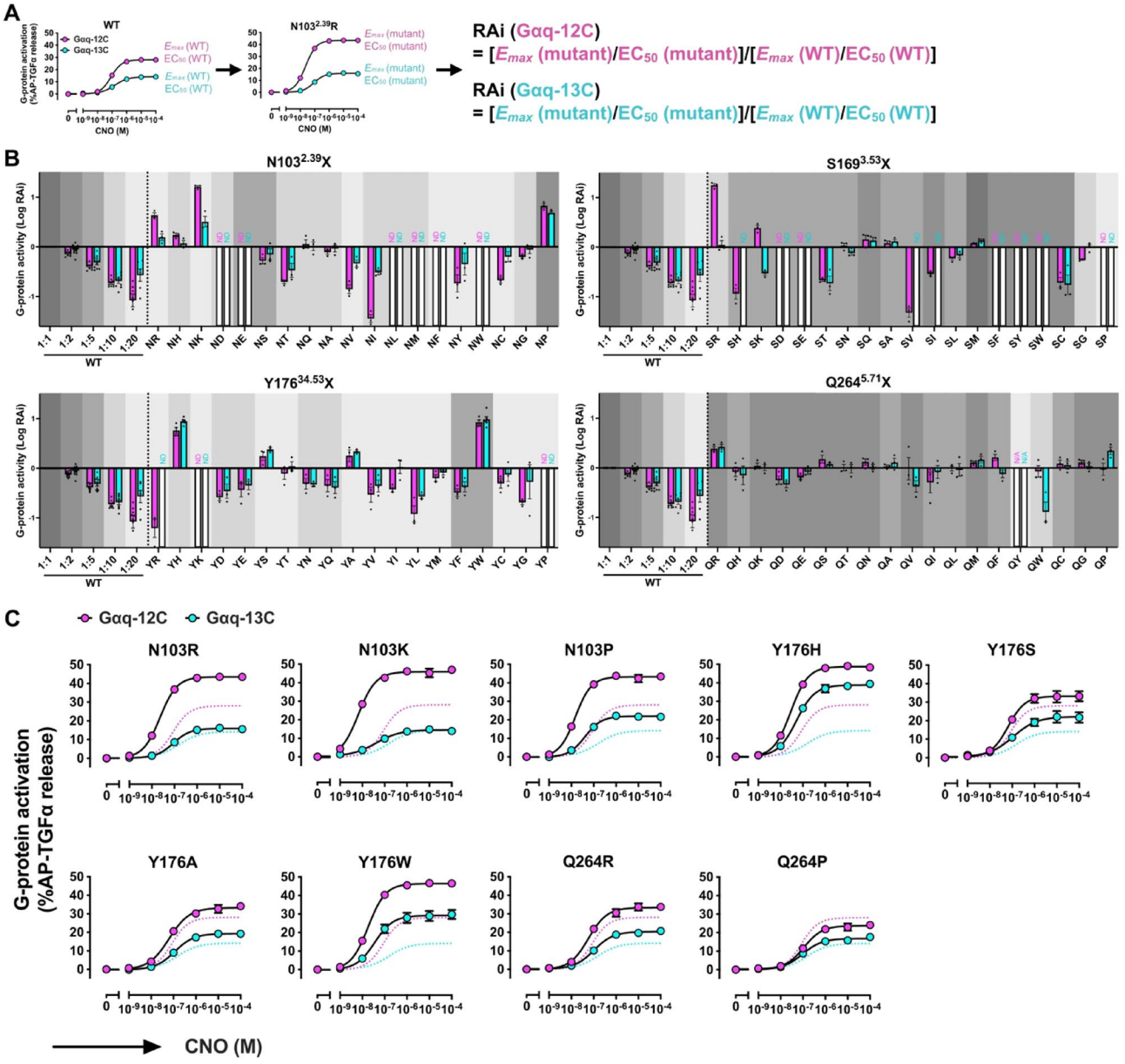

Figure 4. Determining $G_{12}D$ residues involved in the $G\alpha_{12}$-vs-$G\alpha_{13}$ selectivity. (**A**) Calculation method for RAi of the $G_{12}D$ mutants. (**B**) Logarithmic values of RAi of the $G_{12}D$ mutants. $\Delta G_q/\Delta G_{12}$ cells transiently expressing the indicated $G_{12}D$ mutants along with AP-TGFα and $G\alpha_{q\text{-}12C}$ (or $G\alpha_{q\text{-}13C}$) ($G\alpha_{q\text{-}12C}$-expressing condition and $G\alpha_{q\text{-}13C}$-expressing condition are shown as magenta and cyan, respectively). The cell-surface expression levels are shown in gray with different intensities to allow comparison with the wild-type $G_{12}D$. WT (1:2) to (1:20) denote twofold to 20-fold less volumes, respectively, of transfected plasmids than those of the mutant plasmids. Bars and error bars represent the mean and SEM, respectively, for 3–15 independent experiments with each dot representing an individual experiment. The data for WT and its dilutions are reused in all panels. (**C**) Concentration–response curve for the TGFα shedding responses of the representative $G_{12}D$ mutants. The dashed lines represent the responses of the wild-type $G_{12}D$. In all panels, the symbols and error bars represent the mean and SEM, respectively, for three independent experiments. For many data points, the error bars are smaller than the symbols and, thus, are not visible.

and Y176$^{34.53}$W greatly enhanced coupling to $G\alpha_{q\text{-}13C}$, and this enhancement effect was stronger than that for $G\alpha_{q\text{-}12C}$. None of the S169$^{3.53}$ mutations enhanced coupling to $G\alpha_{q\text{-}13C}$, whereas S169$^{3.53}$R and S169$^{3.53}$K selectively enhanced coupling to $G\alpha_{q\text{-}12C}$. Although these mutants of $G_{12}D$ display varying degrees of selective coupling to $G\alpha_{12}$ or $G\alpha_{13}$, the results of these experiments confirm the importance of N103$^{2.39}$, S169$^{3.53}$, Y176$^{34.53}$, Q264$^{5.71}$ as determinants of $G_{12}D$ coupling.

To further enhance coupling between $G\alpha_{13}$ and $G_{12}D$, we introduced additional mutations on top of the Y176$^{34.53}$H mutant, which demonstrated the highest $G\alpha_{13}$-coupling capability in both RAi and E_{max} parameters (Fig. 4B,C, Supplementary Fig. 5–9). We chose N103$^{2.39}$P and Q264$^{5.71}$R because they enhance coupling to $G\alpha_{q\text{-}13C}$ (Fig. 4B,C, Supplementary Fig. 5–9). Compared to Y176$^{34.53}$H, both N103$^{2.39}$R/Y176$^{34.51}$H and Y176$^{34.53}$H/Q264$^{5.71}$R showed increased RAi values under both $G\alpha_{q\text{-}12C}$ and $G\alpha_{q\text{-}13C}$ expressing conditions. Furthermore, Y176$^{34.53}$H/Q264$^{5.71}$R also exhibited an increasing effect on E_{max} (Fig. 5A,B, Supplementary Fig. 10). Based on these results, we designated Y176$^{34.53}$H/Q264$^{5.71}$R double mutant, which exhibits strong coupling to the α5 helices of $G\alpha_{12}$ and $G\alpha_{13}$, as $G\alpha_{12/13}$-DREADD (Fig. 5C).

Discussion

In this study, we showed that I$^{G.H5.23}$ at position G.H5.23 in the α5 helix of $G\alpha_{12}$ is a major determinant of selective coupling between $G\alpha_{12}$ and $G_{12}D$. Conversely, L$^{G.H5.23}$ in $G\alpha_{13}$ has been reported to contribute to the $G\alpha_{13}$ selectivity of GPR35[20]. These findings support the notion that the interaction between G.H5.23 in the α5 helix and target GPCRs is critical for the $G\alpha_{12}$-vs-$G\alpha_{13}$ coupling selectivity. Structural analyses of S1PR2–$G\alpha_{13}$ and GPR35–$G\alpha_{13}$ complexes have revealed that L $^{G.H5.23}$ is oriented toward TM2 and TM3 and is accommodated by a pocket formed by residues 2.39, 3.53, and 34.53[31,32]. In particular, in the S1PR2–$G\alpha_{13}$ complex, ICL2 lies inside the transmembrane core, highlighting the importance of 34.53[31]. These studies support the accuracy of

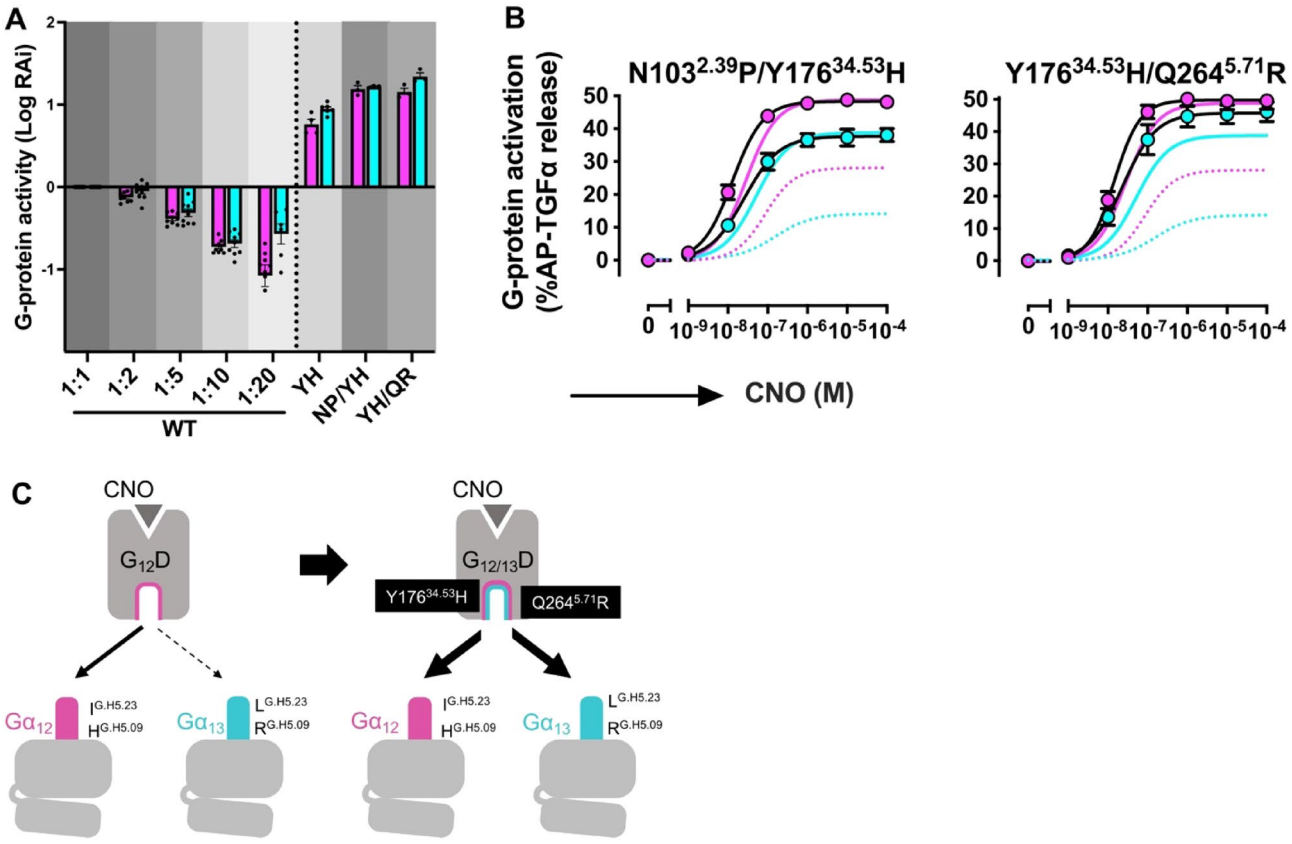

Figure 5. Development of $G\alpha_{12/13}$-DREADD. (**A**) Logarithmic values of RAi of the $G_{12}D$ mutants ($G\alpha_{q\text{-}12C}$ expressing condition = magenta, $G\alpha_{q\text{-}13C}$ expressing condition = cyan). The cell-surface expression levels of the mutants are shown in gray with different intensities to allow comparison with the wild-type $G_{12}D$. WT (1:2) to (1:20) denote twofold to 20-fold less volumes of transfected plasmids, respectively, than those of the mutant plasmids. Bars and error bars represent the mean and SEM, respectively, for three independent experiments performed in triplicate. The data for WT and its dilutions are reused from Fig. 4. (**B**) Concentration–response curve for the TGFα shedding responses of the representative $G_{12}D$ mutants. The dashed lines and solid lines represent the responses of the wild-type $G_{12}D$ and Y176$^{34.53}$H, respectively. In all panels, the symbols and error bars represent the mean and SEM, respectively, for three independent experiments performed in triplicate. For many data points, the error bars are smaller than the symbols and, thus, are not visible. (**C**) A schematic model of the Y176$^{34.53}$H/Q264$^{5.71}$R mutant showing potent coupling to both $G\alpha_{12}$ and $G\alpha_{13}$ via recognition of the three residues in the α5 helix.

our MD-simulated structures of G_{12}D–$G\alpha_{12}$ and G_{12}D–$G\alpha_{13}$ complexes. Notably, the molecular properties of isoleucine and leucine are very similar except for the different positions of the methyl groups in the amino acid side chains, and yet GPCRs distinguish one from the other. This is likely achieved by how well the pocket in the GPCR transmembrane core accommodates the isoleucine versus the leucine side chain. In the MD simulations described in the present study, the methyl group of $G\alpha_{13}$ $L^{G.H5.23}$ is predicted to encounter steric hindrance in the G_{12}D pocket formed by TM2, TM3, and ICL2, which would create instability in the G_{12}D–$G\alpha_{13}$ complex. This idea is consistent with the fact that amino acid substitutions that altered the shape of the transmembrane core of G_{12}D enhanced coupling to $G\alpha_{13}$, presumably by creating a pocket that is optimized to accommodate $L^{G.H5.23}$.

One caveat of this study is that it only identifies determinants of GPCR coupling selectivity in the 26-amino-acid α5 helix of $G\alpha_{12}$ and $G\alpha_{13}$. The rationale for this limitation is that prior studies using chimeric G proteins revealed a crucial role of the α5 helix, especially G.H5.23 and G.H5.24 positions, for determining coupling selectivity[18,19]. By focusing here on the α5 helix, we avoid difficulties arising from differences in the efficiency of the TGFα shedding assay as a surrogate measure of $G\alpha_{12}$- and $G\alpha_{13}$-mediated signaling. However, additional determinants of G protein coupling specificity exist in other protein regions and structures such as the αN–β1 hinge and the β2–β3 loop[33–35]. To fully understand the mechanisms underlying $G\alpha_{12}$-vs-$G\alpha_{13}$-coupling selectivity, a broad examination of determinants of coupling selectivity linked to these elements will be needed in the future. Another caveat is that the present study is based on structural models instead of experimentally verified protein structural data. That said, the full Gα subunit was used in the simulations to ensure that the α5 helix had the proper local environment for positioning relative to the receptor. In addition, to ensure the accuracy of the modeled structures, we performed GaMD followed by clustering before the production runs to ensure that we captured stable conformations of the receptor and the Gα proteins in the modeled complexes. The resulting $G\alpha_{12}$ and $G\alpha_{13}$ simulations showed significant differences in stability. In the future, once the structures of GPCR–$G\alpha_{12}$ or GPCR–$G\alpha_{13}$ complexes are resolved, they can be used to validate and/or improve upon the simulations presented here.

DREADDs that couple specifically to one or more Gα proteins were designed for and have been useful in drug discovery research[36]. $G\alpha_q$-DREADD and $G\alpha_i$-DREADD have been universally used to regulate neuronal activation[37,38]. DREADDs have also been used to analyze G protein signaling in a particular cell population and to predict the effects of agonists that activate specific G-protein-signaling pathways. Administration of CNO to mice genetically modified to express DREADD in a cell type-specific fashion allows for spatio-temporal regulation of specific G-protein signaling. For instance, analyses of DREADD-transgenic mice have revealed the enhancing effect of hepatic glucose production by $G\alpha_s$, $G\alpha_i$, and $G\alpha_q$ signaling in hepatocytes, and our G_{12}D discovered the enhancing effect of browning by $G\alpha_{12}$ signaling in adipocytes[22,39–41]. In the present study, an engineered mutant of G_{12}D created the novel $G\alpha_{12/13}$-DREADD, which is useful for research on $G\alpha_{12/13}$ signaling. In addition, mutations that enhance coupling to $G\alpha_{12}$, including $N103^{2.39}$R, $N103^{2.39}$K, $S169^{3.53}$R, and $S169^{3.53}$K, were discovered in the present study. These mutations could be used to design next-generation G_{12}D that are more potent for $G\alpha_{12}$. $G\alpha_{12}$ and $G\alpha_{13}$ signaling have been reported to have important functions in the immune system. $G\alpha_{12/13}$-coupled GPCRs such as S1PR2 activate $G\alpha_{12/13}$ signaling and regulate immune cell activities and functions in a temporally regulated manner[42,43]. Immune cell species-specific expression of $G\alpha_{12/13}$-DREADD and administration of CNO at various stages of the immune response will aid in a comprehensive understanding of the tightly regulated $G\alpha_{12/13}$ signaling function. However, for functional analysis of $G\alpha_{13}$ signaling alone, future modification of $G\alpha_{12/13}$-DREADD will be necessary to reduce its coupling to $G\alpha_{12}$.

Methods

Reagents and plasmids

CNO dihydrochloride was purchased from Tocris Bioscience or synthesized at the International Institute for Integrative Sleep Medicine (WPIIIIS), University of Tsukuba. The detailed synthetic method was described previously[22]. A plasmid encoding alkaline phosphatase (AP)-TGFα was described previously[5]. G_{12}D (M3D-GPR183/ICL3 $F93^{1.57}$V) and G_{12}D mutants carrying the N-terminal FLAG-epitope tag (DYKDDDDK) were cloned into the pcDNA3.1 expression vector[5]. The amino-acid sequence of FLAG-epitope-tagged G_{12}D is denoted below; the ICL3 swap, the $F93^{1.57}$V mutation, the FLAG-epitope tag and the substitutions of $Y^{3.33}$C and $A^{5.46}$G mutations from the human M3 receptor are underlined and highlighted in bold:

MDYKDDDDKGSTLHNNSTTSPLFPNISSSWIHSPSDAGLPPGTVTHFGSYNVSRAAGNFSSPDGTTD-DPLGGHTVWQVVFIAFLTGILALVTIIGNILVIVS**V**KVNKQLKTVNNYFLLSLACADLIIGVISMNLFTTYI-IMNRWALGNLACDLWLAID**C**VASNASVMNLLVISFDRYFSITRPLTYRAKRTTKRAGVMIGLAWVISFVL-WAPAILFWQYFVGKRTVPPGECFIQFLSEPTITFGTAIAG**F**YMPVTIMTILYWRIYKETE**RTAKQNPLTEKS-GVE**KKAAQTLSAILLAFIITWTPYNIMVLVNTFCDSCIPKTFWNLGYWLCYINSTVNPVCYALCNKTFRT-TFKMLLLCQCDKKKRRKQQYQQRQSVIFHKRAPEQAL.

$G\alpha_{q\text{-}12C}$, $G\alpha_{q\text{-}13C}$, and their mutants were inserted into the pcDNA3.1 expression vector. The amino acid sequence of $G\alpha_{q\text{-}12C}$ and $G\alpha_{q\text{-}13C}$ are as follows (underlining denotes the α5 helices of $G\alpha_{12}$ and $G\alpha_{13}$).

$G\alpha_{q\text{-}12C}$:

MTLESIMACCLSEEAKEARRINDEIERQLRRDKRDARRELKLLLLGTGESGKSTFIKQMRIIHGSGYS-DEDKRGFTKLVYQNIFTAMQAMIRAMDTLKIPYKYEHNKAHAQLVREVDVEKVSAFENPYVDAIK-SLWNDPGIQECYDRRREYQLSDSTKYYLNDLDRVADPAYLPTQQDVLRVRVPTTGIIEYPFDLQSVIFRM-VDVGGQRSERRKWIHCFENVTSIMFLVALSEYDQVLVESDNENRMEESKALFRTIITYPWFQNSSVILFLNK-KDLLEEKIMYSHLVDYFPEYDGPQRDAQAAREFILKMFVDLNPDSDKIIYSHFTCATD**TENVRFVFHAVK-DTILQENLKDIMLQ;**

$G\alpha_{q\text{-}13C}$:

MTLESIMACCLSEEAKEARRINDEIERQLRRDKRDARRELKLLLLGTGESGKSTFIKQMRIIHGSGYSD-EDKRGFTKLVYQNIFTAMQAMIRAMDTLKIPYKYEHNKAHAQLVREVDVEKVSAFENPYVDAIKSLWND-PGIQECYDRRREYQLSDSTKYYLNDLDRVADPAYLPTQQDVLRVRVPTTGIIEYPFDLQSVIFRMVDVG-GQRSERRKWIHCFENVTSIMFLVALSEYDQVLVESDNENRMEESKALFRTIITYPWFQNSSVILFLNKKDL-LEEKIMYSHLVDYFPEYDGPQRDAQAAREFILKMFVDLNPDSDKIIYSHFTCATDTENIRLVFRDVKDTIL-HDNLKQLMLQ.

Cell culture and transfection

Parent and $G\alpha_q/G\alpha_{11}/G\alpha_{12}/G\alpha_{13}$ quadruple-deficient HEK293 cells[5] were maintained in Dulbecco's modified Eagle medium (DMEM, Nissui Pharmaceutical) supplemented with 10% fetal bovine serum (Gibco), 100 U/mL penicillin (Sigma-Aldrich), and 100 µg/mL streptomycin (Gibco) (complete DMEM) in a 37 °C incubator with 5% CO_2. Transfection of plasmid DNAs was performed using lipofection reagent polyethylenimine solution (PEI Max, Polysciences). Typically, cells were seeded in each well of a 12-well culture plate at a cell density of 2×10^5 to 3×10^5 cells/mL in 1 mL complete DMEM and cultured for 1 day in a 37 °C incubator with 5% CO_2. For transfection, plasmid solution was diluted in 50 µL Opti-MEM (Gibco) and mixed with 2.5 µL of 1 mg/mL PEI solution in 50 µL Opti-MEM. Cells were incubated for 1 day after transfection before use in an experiment.

TGFα shedding assay

The TGFα shedding assay was performed as described previously[5,23]. Plasmid transfection was performed in a 12-well plate using a mixture containing 250 ng of plasmid DNA encoding AP-TGFα, 100 ng of plasmid encoding FLAG-G_{12}D, and 50 ng of plasmid encoding $G\alpha_{q\text{-}12C}$ or $G\alpha_{q\text{-}13C}$. After incubation for 1 day, transfected cells were harvested by trypsinization, pelleted by centrifugation at 190 × *g* for 5 min, and suspended in 3.5 mL Hank's Balanced Salt Solution (HBSS) containing 5 mM HEPES (pH 7.4). After incubation for 15 min at room temperature, during which spontaneous AP-TGFα shedding settled down, the cells were centrifuged at 190 × *g* for 5 min, and cell pellets were resuspended in 3.5 mL HBSS. The resuspended cells were plated in a 96-well plate at 90 µl per well (typically 24 total wells; triplicate measurement) and placed in a 37 °C incubator with 5% CO_2 for 30 min. After incubation, 10 µl of 10× CNO serial dilution in HBSS containing 5 mM HEPES (pH 7.4) and 0.01% (v/w) bovine serum albumin (BSA) was added to each well and incubated for 1 h at 37 °C in 5% CO_2. The 96-well cell plates were centrifuged at 190 × *g* for 2 min. After centrifugation, 80 µL supernatant from each well was transferred to another 96-well plate (conditioned media plate or CM plate), leaving attached cells and 20 µL supernatant in the original well of the cell plate. Then, 80 µL of para-nitrophenyl phosphate (*p*-NPP) solution (10 mM *p*-NPP; 40 mM Tris-HCl, pH 9.5; 40 mM NaCl; 10 mM $MgCl_2$) was added to each well of each plate. Absorbance at 405 nm (Abs_{405}) was measured for both plates before (background) and after a 1-h or 2-h incubation at room temperature using a microplate reader (SpectraMax 340 PC384, Molecular Devices). The percent of AP-TGFα release was calculated using the following equation:

$$\text{AP-TGF}\alpha\ (\%\ \text{CM}) = [\Delta \text{Abs}_{405\ \text{CM}} / (\Delta \text{Abs}_{405\ \text{CM}} + \Delta \text{Abs}_{405\ \text{cell}}) \times 1.25] \times 100$$

where CM denotes conditioned media.

Vehicle-treated AP-TGFα (%CM) was subtracted from CNO-stimulated AP-TGFα (%CM) and the resulting value (%AP-TGFα release) was used to represent a G-protein response.

Flow cytometry

$\Delta Gq/\Delta G_{12}$ cells were seeded in a 12-well culture plate at a concentration of 3×10^5 cells per mL (1 mL per well) 1 day before transfection. Transfection was performed using 100 ng of plasmid encoding FLAG-G_{12}D (or mutant FLAG-G_{12}D), 250 ng plasmid encoding AP-TGFα and 50 ng plasmid encoding $G\alpha_{q\text{-}12C}$ (or $G\alpha_{q\text{-}13C}$). After incubation for 1 day, cells were collected by adding 100 µL 0.53 mM EDTA-containing D-PBS, followed by 100 µL of 5 mM HEPES (pH 7.4)-containing HBSS. The cell suspension was transferred to a 96-well V-bottom plate and fluorescently labeled using anti-FLAG-epitope tag monoclonal antibody (Clone 1E6, FujiFilm Wako Pure Chemical; 10 µg per mL) diluted in 2% goat serum, 2 mM EDTA in D-PBS (blocking buffer), followed by goat anti-mouse IgG secondary antibody conjugated with Alexa Fluor 488 (Thermo Fisher Scientific; 10 µg per mL). After washing with D-PBS, the cells were resuspended in 200 µL of 2 mM EDTA in D-PBS and filtered through a 40-µm filter. Single-cell fluorescence was quantified using an EC800 flow cytometer with a 488-nm laser (Sony). Live cells were gated with a forward scatter ('FS-Peak-Lin') cutoff of 390 and a gain of 1.7. Mean fluorescence intensity of all recorded events (approximately 20,000 cells per sample) was analyzed with FlowJo software (FlowJo) and used for statistical analysis.

Western blot

$\Delta G\alpha_q/\Delta G_{12}$ cells were lysed in SDS-PAGE sample buffer (62.5 mM Tris–HCl [pH 6.8], 50 mM dithiothreitol, 2% SDS, 10% glycerol, and 4 M urea) containing 1 mM EDTA, 1 mM phenylmethylsulfonyl fluoride and 2 mM sodium orthovanadate. Lysates of an equal number of cells were separated using 8% or 12.5% SDS-polyacrylamide gel electrophoresis. Subsequently, the proteins were transferred to a nitrocellulose membrane (GE Healthcare). The membrane was blocked in 5% skim milk in blotting buffer (10 mM Tris–HCl (pH 7.4), 190 mM NaCl, and 0.05% Tween 20), and proteins were labeled and visualized by immunoblotting with appropriate primary and secondary antibodies. The primary antibody used in this study was an anti-G_q goat polyclonal antibody (Abcam, ab128060, D-6, lot GR108939-6, 1:2000 dilution). The secondary antibody was horseradish peroxidase (HRP)-conjugated anti-goat IgG (American Qualex, A201PS lot 7A0327H). The membrane was soaked in luminol reagent (100 mM Tris–HCl (pH 8.5), 50 mg per mL of Luminol Sodium Salt HG (FujiFilm Wako Pure

Chemical), 0.2 mM *p*-Coumaric acid and 0.03% (v/v) of H_2O_2). Chemiluminescence imaging was performed and band intensities were measured using Amersham Imager 680 (Cytiva).

Modeling the G_{12}D–Gα_{12} and the G_{12}D–Gα_{13} complexes

To build computational models of the G_{12}D–Gα_{12} and the G_{12}D–Gα_{13} complexes, we used SWISS-MODEL and I-TASSER structure prediction software packages with the muscarinic acetylcholine receptor 1 (M1R)–G_{11} protein complex (PDB: 6OIJ) as a template [24–26] (Fig. 2A). These predicted structures were embedded in a phosphatidylcholine lipid bilayer using the Bilayer Builder tool in CHARMM-GUI[27].

Molecular dynamics simulation and clustering

Each complex was relaxed and equilibrated through 500-ns NPT ensemble conventional molecular dynamics (cMD) simulations using a 2-fs time step, an AMBER force field, and AMBER's pmemd.cuda program[44]. For the duration of all simulations, pressure and temperature were kept at 1 atm and 310.15 K, respectively. Before full-length cMD simulations, both complexes underwent six relaxation steps to minimize energy and equilibrate the systems as described previously[28]. G_{12}D–Gα_{12} and G_{12}D–Gα_{13} complexes were then subjected to 50-ns GaMD equilibration followed by a 500-ns GaMD production run using default parameters, which includes harmonic dual-boost potential to reduce energy barriers to enhance conformational sampling[29]. To find distinct conformations in the GaMD snapshots, the DBScan clustering algorithm was used with the "*minpoints*" parameter set to 4 conformations and the distance cutoff "*epsilon*" parameter of 2.25 Å[45]. The full receptor–Gα complex was aligned during clustering. The DBScan clustering algorithm used pairwise-RMSD of this complex between any two trajectory snapshots as the distance metric for clustering. Any two conformation with an RMSD greater than 2.25 Å is put in different clusters and all final reported clusters should have at least 4 conformations in each cluster based on the parameters used. The advantage of this algorithm over other popular algorithms like K-means clustering and hierarchical clustering is that in DBScan clustering one does not need to specify the target number of clusters, because the number of clusters should be determined by the underlying dynamics of the molecular system. The conformation that best represented each DBScan cluster as its centroid was chosen as a starting point for an additional 500-ns cMD simulation to allow for unbiased MMPBSA energy calculations and analysis of receptor–G-protein interactions. Residue interaction analysis was performed on the average structure of the most populated cluster for each complex.

Receptor–Gα binding free energy analysis

MMPBSA-based total energy (ΔG) was determined by calculating the difference between the complex free energy and the sum of the G protein and receptor free energies as described previously[28].

Data analysis

Concentration–response curves were fitted using Nonlinear Regression Analysis: Variable slope (four parameters) function in the GraphPad Prism 9 software (GraphPad) was used with absolute Hill Slope values less than 2. Sigmoid maximum effect (E_{max}, also referred to as Span) and the negative log of the half-maximal excitation concentration (pEC_{50}) were used to evaluate G-protein-coupling activity. Protocols for normalizing and for generating experimental replicates are described in the legends of each Figure, as appropriate.

Data availability

All data generated or analyzed in study are provided in the separated Source Data file in Supplementary information file section.

Received: 20 November 2023; Accepted: 7 May 2024
Published online: 15 May 2024

References

1. Pierce, K. L., Premont, R. T. & Lefkowitz, R. J. Seven-transmembrane receptors. *Nat. Rev. Mol. Cell Biol.* **3**, 639–650 (2002).
2. Hauser, A. S., Attwood, M. M., Rask-Andersen, M., Schiöth, H. B. & Gloriam, D. E. Trends in GPCR drug discovery: New agents, targets and indications. *Nat. Rev. Drug Discov.* **16**, 829–842 (2017).
3. Wettschureck, N. & Offermanns, S. Mammalian G proteins and their cell type specific functions. *Physiol. Rev.* **85**, 1159–1204 (2005).
4. Alexander, S. P. *et al.* The concise guide to PHARMACOLOGY 2021/22: G protein-coupled receptors. *Br. J. Pharmacol.* **178**(Suppl 1), S27–S156 (2021).
5. Inoue, A. *et al.* Illuminating G-protein-coupling selectivity of GPCRs. *Cell* **177**, 1933-1947.e25 (2019).
6. Ono, Y. *et al.* Generation of Gαi knock-out HEK293 cells illuminates Gαi-coupling diversity of GPCRs. *Commun. Biol.* **6**, 112 (2023).
7. Buhl, A. M., Johnson, N. L., Dhanasekaran, N. & Johnson, G. L. Gα_{12} and Gα_{13} stimulate Rho-dependent stress fiber formation and focal adhesion assembly. *J. Biol. Chem.* **270**, 24631–24634 (1995).
8. Ruppel, K. M. *et al.* Essential role for Gα_{13} in endothelial cells during embryonic development. *Proc. Natl. Acad. Sci. U. S. A.* **102**, 8281–8286 (2005).
9. Offermanns, S., Mancino, V., Revel, J. P. & Simon, M. I. Vascular system defects and impaired cell chemokinesis as a result of Gα_{13} deficiency. *Science* **275**, 533–536 (1997).
10. Gu, J. L., Müller, S., Mancino, V., Offermanns, S. & Simon, M. I. Interaction of Gα_{12} with Gα_{13} and Gα_q signaling pathways. *Proc. Natl. Acad. Sci. U. S. A.* **99**, 9352–9357 (2002).
11. Liu, G., Han, J., Profirovic, J., Strekalova, E. & Voyno-Yasenetskaya, T. A. Gα_{13} regulates MEF2-dependent gene transcription in endothelial cells: Role in angiogenesis. *Angiogenesis* **12**, 1–15 (2009).
12. Vaiskunaite, R., Kozasa, T. & Voyno-Yasenetskaya, T. A. Interaction between the Gα subunit of heterotrimeric G_{12} protein and Hsp90 is required for Gα_{12} signaling. *J. Biol. Chem.* **276**, 46088–46093 (2001).

13. Shi, C. S., Sinnarajah, S., Cho, H., Kozasa, T. & Kehrl, J. H. $G_{13}\alpha$-mediated PYK2 activation. PYK2 is a mediator of $G_{13}\alpha$-induced serum response element-dependent transcription. *J. Biol. Chem.* **275**, 24470–24476 (2000).
14. Hauser, A. S. *et al.* Common coupling map advances GPCR-G protein selectivity. *Elife* **11**, e74107 (2022).
15. Armstrong, J. F. *et al.* The IUPHAR/BPS guide to PHARMACOLOGY in 2020: Extending immunopharmacology content and introducing the IUPHAR/MMV guide to MALARIA PHARMACOLOGY. *Nucleic Acids Res.* **48**, D1006–D1021 (2020).
16. Avet, C. *et al.* Effector membrane translocation biosensors reveal G protein and βarrestin coupling profiles of 100 therapeutically relevant GPCRs. *Elife* **11**, e74101 (2022).
17. Rasmussen, S. G. F. *et al.* Crystal structure of the β_2 adrenergic receptor-Gs protein complex. *Nature* **477**, 549–555 (2011).
18. Conklin, B. R., Farfel, Z., Lustig, K. D., Julius, D. & Bourne, H. R. Substitution of three amino acids switches receptor specificity of $G_q\alpha$ to that of $G_i\alpha$. *Nature* **363**, 274–276 (1993).
19. Conklin, B. R. *et al.* Carboxyl-terminal mutations of $G_q\alpha$ and $G_s\alpha$ that alter the fidelity of receptor activation. *Mol. Pharmacol.* **50**, 885–890 (1996).
20. Mackenzie, A. E. *et al.* Receptor selectivity between the G proteins $G\alpha_{12}$ and $G\alpha_{13}$ is defined by a single leucine-to-isoleucine variation. *FASEB J.* **33**, 5005–5017 (2019).
21. Armbruster, B. N., Li, X., Pausch, M. H., Herlitze, S. & Roth, B. L. Evolving the lock to fit the key to create a family of G protein-coupled receptors potently activated by an inert ligand. *Proc. Natl. Acad. Sci. U. S. A.* **104**, 5163–5168 (2007).
22. Ono, Y. *et al.* Chemogenetic activation of G_{12} signaling enhances adipose tissue browning. *Signal Transduct. Target. Ther.* **8**, 307 (2023).
23. Inoue, A. *et al.* TGFα shedding assay: An accurate and versatile method for detecting GPCR activation. *Nat. Methods* **9**, 1021–1029 (2012).
24. Waterhouse, A. *et al.* SWISS-MODEL: Homology modelling of protein structures and complexes. *Nucleic Acids Res.* **46**, W296–W303 (2018).
25. Yang, J. & Zhang, Y. I-TASSER server: New development for protein structure and function predictions. *Nucleic Acids Res.* **43**, W174–W181 (2015).
26. Maeda, S., Qu, Q., Robertson, M. J., Skiniotis, G. & Kobilka, B. K. Structures of the M1 and M2 muscarinic acetylcholine receptor/G-protein complexes. *Science* **364**, 552–557 (2019).
27. Jo, S., Kim, T., Iyer, V. G. & Im, W. CHARMM-GUI: A web-based graphical user interface for CHARMM. *J. Comput. Chem.* **29**, 1859–1865 (2008).
28. Santiago, L. J. & Abrol, R. Understanding G protein selectivity of muscarinic acetylcholine receptors using computational methods. *Int. J. Mol. Sci.* **20**, 5290 (2019).
29. Miao, Y., Feher, V. A. & McCammon, J. A. Gaussian accelerated molecular dynamics: Unconstrained enhanced sampling and free energy calculation. *J. Chem. Theory Comput.* **11**, 3584–3595 (2015).
30. Botello-Smith, W. M. & Luo, R. Applications of MMPBSA to membrane proteins I: Efficient numerical solutions of periodic Poisson–Boltzmann equation. *J. Chem. Inf. Model.* **55**, 2187–2199 (2015).
31. Chen, H. *et al.* Structure of S1PR2-heterotrimeric G_{13} signaling complex. *Sci. Adv.* **8**, eabn0067 (2022).
32. Duan, J. *et al.* Insights into divalent cation regulation and G_{13}-coupling of orphan receptor GPR35. *Cell Discov.* **8**, 135 (2022).
33. Chung, K. Y. *et al.* Conformational changes in the G protein Gs induced by the β_2 adrenergic receptor. *Nature* **477**, 611–615 (2011).
34. Zhang, M. *et al.* Cryo-EM structure of an activated GPCR-G protein complex in lipid nanodiscs. *Nat. Struct. Mol. Biol.* **28**, 258–267 (2021).
35. Jelinek, V., Mösslein, N. & Bünemann, M. Structures in G proteins important for subtype selective receptor binding and subsequent activation. *Commun. Biol.* **4**, 635 (2021).
36. Meister, J., Wang, L., Pydi, S. P. & Wess, J. Chemogenetic approaches to identify metabolically important GPCR signaling pathways: Therapeutic implications. *J. Neurochem.* **158**, 603–620 (2021).
37. Rogan, S. C. & Roth, B. L. Remote control of neuronal signaling. *Pharmacol. Rev.* **63**, 291–315 (2011).
38. Roth, B. L. DREADDs for neuroscientists. *Neuron* **89**, 683–694 (2016).
39. Akhmedov, D. *et al.* Gs-DREADD knock-in mice for tissue-specific, temporal stimulation of cyclic AMP signaling. *Mol. Cell. Biol.* **37**, e00584-16 (2017).
40. Rossi, M. *et al.* Hepatic G_i signaling regulates whole-body glucose homeostasis. *J. Clin. Invest.* **128**, 746–759 (2018).
41. Li, J. H. *et al.* A novel experimental strategy to assess the metabolic effects of selective activation of a G_q-coupled receptor in hepatocytes in vivo. *Endocrinology* **154**, 3539–3551 (2013).
42. Green, J. A. *et al.* The sphingosine 1-phosphate receptor $S1P_2$ maintains the homeostasis of germinal center B cells and promotes niche confinement. *Nat. Immunol.* **12**, 672–680 (2011).
43. Moriyama, S. *et al.* Sphingosine-1-phosphate receptor 2 is critical for follicular helper T cell retention in germinal centers. *J. Exp. Med.* **211**, 1297–1305 (2014).
44. Case, D. A. *et al.* The Amber biomolecular simulation programs. *J. Comput. Chem.* **26**, 1668–1688 (2005).
45. Roe, D. R. & Cheatham, T. E. PTRAJ and CPPTRAJ: Software for processing and analysis of molecular dynamics trajectory data. *J. Chem. Theory Comput.* **9**, 3084–3095 (2013).

Acknowledgements

We thank Ayaki Saito and other members of the Inoue laboratory for helpful discussion and manuscript editing; Kayo Sato, Shigeko Nakano and Ayumi Inoue (Tohoku University) for their assistance in plasmid preparation; Tsuyoshi Saitoh (Tsukuba University) for kindly providing CNO. AI was funded by KAKENHI JP21H04791, JP21H05113, JPJSBP120213501 and JPJSBP120218801 from Japan Society for the Promotion of Science (JSPS); JPMJFR215T, JPMJMS2023 and 22714181 from Japan Science and Technology Agency (JST); JP22ama121038 and JP22zf0127007 from the Japan Agency for Medical Research and Development (AMED); Takeda Science Foundation. MT received JSPS KAKENHI 22J10475. This work was also supported in part by the SCORE2 grant SC2GM130480 to RA from the United States National Institutes of Health.

Author contributions

Conceptualization, M.T. and A.I., Investigation, M.T., C.C., N.K., R.K., G.N. and T.I.; Writing, M.T., C.C. and A.I. with feedback from all of the coauthors; Funding Acquisition, M.T., A.I. and R.A.; Supervision, R.A. and A.I.

Competing interests

The authors declare no competing interests.

Additional information

Supplementary Information The online version contains supplementary material available at https://doi.org/10.1038/s41598-024-61506-4.

Correspondence and requests for materials should be addressed to A.I.

Reprints and permissions information is available at www.nature.com/reprints.

Publisher's note Springer Nature remains neutral with regard to jurisdictional claims in published maps and institutional affiliations.